13th International Symposium on Turbulence and Shear Flow Phenomena (TSFP13)
Montreal, Canada, June 25-28, 2024

Dissipation Scaling in Production Region of Fractal Grid Turbulence

Amir Sagharichi
Department of Mechanical Engineering
University of Manitoba
Winnipeg, Manitoba, R3T 5V6, Canada
Sagharia@myumanitoba.ca

Mark F. Tachie
Department of Mechanical Engineering
University of Manitoba
Winnipeg, Manitoba, R3T 5V6, Canada
mark.tachie@umanitoba.ca

ABSTRACT

The turbulence energy dissipation rate (C_ε) and turbulence Reynolds number (Re_λ) in the cross-stream directions in the wake of fractal grids are investigated using high-resolution particle image velocimetry (PIV). The grids include two fractal square grids with blockage ratios of 32% and 41%. The PIV measurements were conducted in the production, peak, and decay regions, and the data were analyzed in terms of the mean velocity, turbulence intensity, small- and large-scale isotropy, invariant of velocity gradient tensor, and energy dissipation rate coefficient. The analyses of isotropy as well as the probability density function of velocity and vorticity fluctuation in the production region and peak location along the cross-stream direction reveal inhomogeneous and anisotropic turbulence characteristics, irrespective of the blockage ratio. The results show that data in the production region and peak location adhere to a non-equilibrium turbulence energy dissipation rate scaling, however, this scaling is different from the traditional non-equilibrium equation which relates the local (Re_λ) and global (Re_0) Reynolds numbers and turbulence energy dissipation rate coefficient ($C_\varepsilon \propto {Re_0^{m/2}}/{Re_\lambda^n}$; with $n = m \approx 1$) along the grid's centerline. It is shown that the turbulence dissipation rate coefficient in the production region and peak location of fractal grids ($C_{\epsilon'}$) can be related to a newly defined local Reynolds number ($Re_{\lambda'}$) and global Reynolds number (Re_L) through $C_{\epsilon'}Re_{\lambda'} \propto {1}/{Re_L^{0.2}}$.

INTRODUCTION

Grid turbulence is an important topic in the turbulence research community, as it is the best representative of homogenous isotropic turbulence (Yao et al., 2021). Besides its fundamental importance, turbulence-generating grids are also used in diverse engineering applications. For instance, grids are used as turbulators to enhance thermal mixing (Laizet and Vassilicos, 2012), in fluidic energy harvesting (Ferko et al., 2019), impinging jets for efficient enhancement of heat transfer (Cafiero et al., 2021), and spoilers for mitigating vortex shedding and acoustic emissions (Nedić and Vassilicos, 2015). Thus, a thorough understanding of grid turbulence is essential for the design of innovative control strategies for diverse fluid and thermal devices. Grid turbulence can be produced using either passive (regular and fractal) or active grids (Poorte and Biesheuvel, 2002; Nagata et al., 2013; and Azzam and Lavoie, 2023). The investigation of turbulence generated by regular and fractal grids by Hurst and Vassilicos (2007) over 21 different grids showed that, regardless of the geometry, the flow downstream of the grids is characterized by an inhomogeneous and anisotropic region in the vicinity of the grids, where turbulence is produced. This region is followed by a peak in turbulence and a decay region where the flow is approximately homogeneous and isotropic.

One of the fundamental aspects of grid turbulence is the Taylor–Kolmogorov dissipation scaling theory, which states that in the decay region, the turbulence kinetic energy (TKE) dissipation rate coefficient (C_ε) is constant and independent of the turbulence Reynolds number ($Re_\lambda = {u_{rms}\lambda}/{\nu}$, where $u_{rms} = \sqrt{\overline{u^2}}$ is root-mean-square of the streamwise fluctuating velocity u', $(\overline{.})$ denotes time averaging, $\lambda = \sqrt{{2u_{rms}^2}/{\overline{(\frac{\partial u'}{\partial x})^2}}}$ is the longitudinal Taylor microscale, and ν is fluid kinematic viscosity):

$$C_\varepsilon = {\varepsilon L_u}/{u_{rms}^3} \approx \text{Constant} \qquad (1)$$

In Equation 1, ε is the TKE dissipation per unit mass, and L_u is the longitudinal integral length scale. Equation 1, which is often referred to as 'equilibrium scaling' presupposes that the mechanism of energy transfer between different scales of turbulence motions is in a state of equilibrium (Goto and Vassilicos, 2016; Chen et al., 2021). This concept forms the basis for the formulation of turbulence models in Reynolds-averaged Navier-Stokes (RANS) equations, as it offers a direct approach to estimate the TKE dissipation rate (Pope, 2000). The TKE dissipation rate can be estimated under the assumption of local isotropy, as outlined in Pope (2000):

$$\varepsilon = {15\nu\, u_{rms}^2}/{\lambda^2} \qquad (2)$$

It follows from Equations 1 and 2 that the equilibrium scaling can be expressed as Equation 3 which indicates that there is a direct relationship between L_u/λ and Re_λ.

$${L_u}/{\lambda} = \frac{C_\varepsilon}{15} Re_\lambda \approx \text{Constant} \qquad (3)$$

Valente and Vassilicos (2015) observed that in the initial decay region of grid turbulence, the turbulence dissipation rate coefficient does not adhere to a constant value as described in Equation 3. Instead, C_ε varies with both the global Reynolds number (Re_0) and local Reynolds numbers (Re_λ) as follows (Vassilicos, 2015):

$$C_\varepsilon \propto {Re_0^{m/2}}/{Re_\lambda^n} \; (\neq \text{Constant}) \qquad (4)$$

Here, the empirical exponents $m \approx n \approx 1$ and $Re_0 = {U_\infty t_0}/{\nu}$ is Reynolds number based on the freestream velocity (U_∞) and grids' largest bar thickness (t_0). This observation, which was also made in the flow downstream of active grids (Zheng et al., 2023), is referred to as the 'non-equilibrium turbulence dissipation scaling' and has been attributed to the residual strain in the near field of the grids (Isaza et al., 2014). The non-

equilibrium scaling has also found widespread application in both homogeneous and inhomogeneous turbulence, including turbulent boundary layers (Obligado et al., 2022), free jets (Cafiero and Vassilicos, 2019), and wake of a slender body (Ortiz-Tarin et al., 2021). Despite the widespread applicability of Equation 4, the precise values of the exponents (m and n) are subject to debate. Bos and Rubinstein (2017) obtained m = n = 15/14 for regular and fractal grids under the assumption that the flow is homogenous and isotropic and introduced a new scaling as follows:

$$C_\varepsilon/C_{\varepsilon 0} \propto (Re_\lambda/Re_{\lambda 0})^{\frac{-15}{14}} \quad (5)$$

where $C_{\varepsilon 0}$ and $Re_{\lambda 0}$ are the equilibrium values of C_ε and Re_λ. Chen et al. (2021) argued that these values can be influenced by inhomogeneity. Zheng et al. (2021) demonstrated that the scaling proposed by Bos and Rubinstein (2017) holds in the flow downstream of active grids with an equilibrium value of $C_{\varepsilon 0} = 0.81$, which is in good agreement with 0.87 (Puga et al., 2017) and 0.82 (Kang et al., 2003).

The scaling of the TKE dissipation rate coefficient plays a significant role in turbulence research including the growth rate of self-similar turbulence jets and wakes, which is highly dependent on C_ε (Cafiero and Vassilicos, 2019). It has been shown that non-equilibrium turbulence dissipation scaling holds along the centerline of passive and active grids (Hearst, 2015; Zheng et al., 2023). However, there is a knowledge gap on the applicability of non-equilibrium relations in the cross-stream direction in the production region, where small- and large-scale structures interact nonlinearly to generate turbulence. This knowledge gap has constrained our comprehension of the dynamics of grid-induced turbulence. Also, the universality of the relationship between C_ε and Re_λ in the cross-stream direction in turbulent flows characterized by inhomogeneity and anisotropy has not yet been established. Thus, the objective of this study is to assess the validity of the non-equilibrium TKE dissipation scaling in the cross-stream direction within the inhomogeneous and anisotropic region downstream of two fractal grids using PIV.

EXPERIMENTAL PROCEDURE

The experiments were performed in a recirculating open water tunnel with a test section of 600 mm in width, 450 mm in height, and 6000 mm in length. Two square fractal grids with blockage ratios (σ) of 32% (denoted as F32) and 41% (denoted as F41) with a streamwise thickness of 6.5 mm were fabricated from stainless steel and placed at the inlet of the test section to cover the entire cross-section of the channel. The grid design follows a square shape and incorporates N = 3 iterations of fractal patterns. The grids' schematics and pertinent geometrical specifications are presented in Figure 1 and Table 1, respectively.

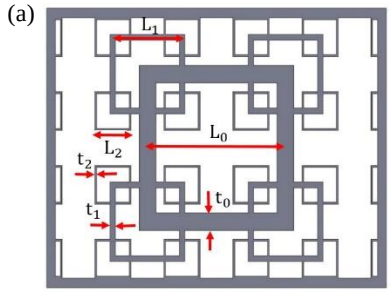

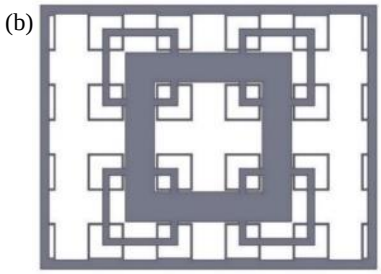

Figure 1. Schematic of turbulence generating grids: (a) F32, and (b) F41.

Table 1. Grids specifications.

Parameters	F32	F41
N	3	3
t_r	9.50	17
L_0 (mm)	238	238
L_1 (mm)	119	119
L_2 (mm)	59.50	59.50
t_0 (mm)	28.50	51
t_1 (mm)	9.25	12.37
t_2 (mm)	3	3
t_0/L_0	0.12	0.21
σ %	32	41

The freestream velocity was set to $U_\infty = 0.25$ (m/s) at the inlet section of the tunnel which led to Reynolds number $Re_0 = 7125$ and 12750 for F32, and F41, respectively.

Double-frame PIV was implemented to measure the velocity vectors within the flow field. Silver-coated hollow glass spheres of mean diameter of $d_p = 10$ μm and density of $\rho_p = 1400$ kg m^{-3} were introduced into the flow as seeding particles. To assess the ability of the particles to accurately follow the flow, the Stokes number (S_t) of the particles was determined by comparing the particle response time (τ_p) to the characteristic temporal scale in the flow (τ_f). The particle response time was found to be $\tau_p = 2.2 \times 10^{-6}$. The characteristic temporal scale was determined as the minimum value of $\tau_f = \sqrt{\nu/\varepsilon}$ in the near field, and the values of the Stokes number were found to be $S_t = 6.27 \times 10^{-5}$ and 9.80×10^{-5} for the F32 and F41 grids, respectively. Since these values are significantly lower than the critical value of 0.05 proposed by Samimy and Lele (1991), it was concluded that the seeding particles faithfully respond to changes in the flow motion. The flow field was illuminated by a Photonics DM30-527DH dual-cavity dual-head high-speed neodymium-doped yttrium lithium fluoride (Nd: YLF) laser. The wavelength and the maximum energy output of each laser pulse are 532 nm and 30 mJ/pulse, respectively. To mitigate laser distortion induced by surface bubbles emerging from the hydraulic drop downstream of the grids, a 9 mm thick acrylic surface plate, measuring 576 mm in length, was positioned beneath the laser, submerged below the free surface. Two side-by-side Complementary Metal Oxide Semiconductor (CMOS) cameras (2560 pixel × 1600 pixel) placed perpendicular to the sidewall of the channel to capture the illuminated particles. Each camera image covers an area of 323 mm × 202 mm resulting in an image magnification of 126 μm /pixel. A total of 12 000 snapshots were obtained at a sampling frequency of 3 Hz for each test case. The measurements were performed at the channel midspan plane. Davis (version 10.2) supplied by LaVision Inc. was used for data acquisition and vector calculation. The velocity vectors were calculated using a

GPU-accelerated multi-pass cross-correlation algorithm, with an initial interrogation window of 128 pixels × 128 pixels with 50% overlap followed by final four passes with an interrogation window of 24 pixels × 24 pixels and 75% overlap.

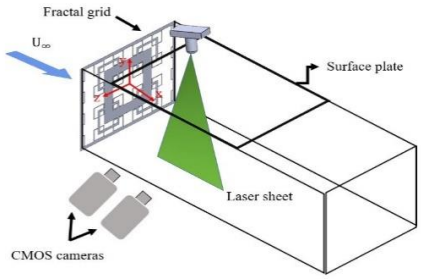

Figure 2. Schematic of the experimental setup.

The spatial resolution of the PIV measurement plays a crucial role in obtaining a reliable estimate of the energy dissipation rate (Chen et al., 2021). For a reliable estimate of the TKE dissipation rate, Tokgoz et al. (2012) suggested that the ratio of the interrogation window size (Δd) to the Kolmogorov length scale $\eta\ (=(\nu^3/\varepsilon)^{1/4}$, where ε was calculated using Equation 2) should not exceed 6 to 8 if a 75% overlap of interrogation window was implemented. It is observed from Figure 3 that the ratio $\Delta d/\eta$ along the grid centerline ranges from 2 to 5 for both grids. Hence, the spatial resolution is deemed sufficient for the estimation of the energy dissipation rate.

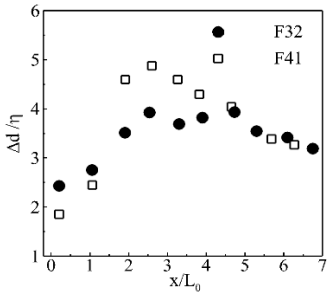

Figure 3. The ratio of the interrogation window size to the Kolmogorov length scale along the grid's centerline.

RESULTS AND DISCUSSION

Mean flow characteristics

To characterize the mean flow downstream of the grids, Figure 4 displays the plots of the streamwise mean velocity with mean streamlines superimposed. Downstream of the grids, the mean flow exhibits regions of high velocity resembling jet-like structures. Furthermore, the flow downstream of the F41 grid demonstrates greater momentum compared to the F32 grid, which can be attributed to the higher blockage ratio in the former case. Figure 5 illustrates the distribution of the normalized streamwise mean velocity along the centerline (U_c). In the case of F32, the peak centerline velocity occurs at x/L_0 = 0.35 which is half of the corresponding value for F41. For F32 and F41, the peak centerline value is U_c/U_∞ = 1.75 and 2.60, respectively. Following the peak, the mean velocity along the centerline decays gradually to U_c/U_∞ = 1. The velocity recovery rate is faster for F41 compared to F32.

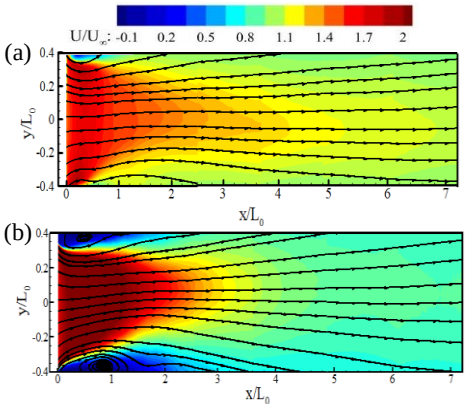

Figure 4. Contours of normalized streamwise mean velocity superimposed by mean streamlines for F32 (a), and F41 (b).

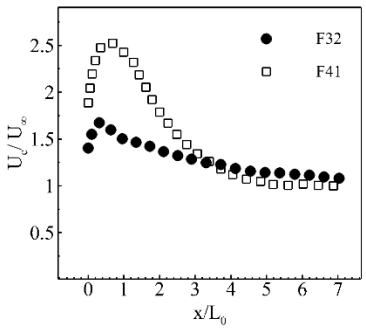

Figure 5. Normalized streamwise mean velocity distribution along the grid centerline.

Figure 6 shows the distribution of the streamwise turbulence intensity ($T_u = u_{rms}/U_\infty$) along the grid's centerline. Downstream of the grids, turbulence intensity rapidly increases to reach its peak value at x/L_0 = 3.12 and 2.01 for F32 and F41, respectively. The peak value of turbulence intensity for F41 and F32 is T_u = 46% and 15%, respectively. This difference can be attributed to the larger bar thickness which leads to stronger wake interaction downstream of the F41 grid compared to the F32 grid. Although turbulence intensity decays thereafter, it remains higher in the F41 grid compared to the F32. Figure 6b compares the centerline streamwise turbulence intensity with relevant literature. The figure demonstrates a good agreement between the present and previous results.

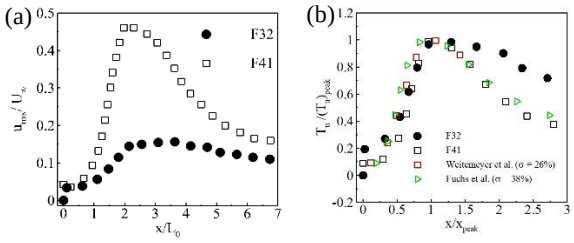

Figure 6. Streamwise development of streamwise turbulence intensity (a), comparison with literature (b).

It is well documented that the flow near the grid is inhomogeneous and anisotropic, which can be attributed to the existence of coherent structures that dominate the production region (Melina et al., 2016). To assess the global isotropy downstream of the grids, the streamwise evolution of u_{rms}/V_{rms} along the grid's centerline is shown in Figure 7 (in this figure x_{peak} is the streamwise location where T_u peaks).

The flow in the proximity to the grids exhibits significant anisotropy with values of u_{rms}/v_{rms} as high as 1.47 and as low as 0.96. The global isotropy, however, tends to improve with streamwise distance, and it lies between 1.15 - 1.22 for $x/x_{peak} \geq 1$ which is in good agreement with u_{rms}/v_{rms} = 1.10 - 1.25 reported by Hurst and Vassillicos (2007).

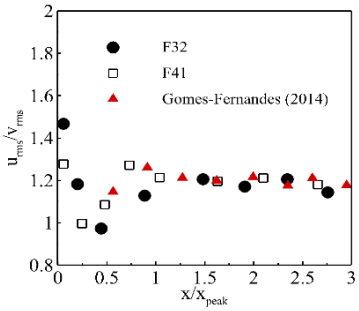

Figure 7. Streamwise evolution of global isotropy along the grid centerline.

Flow characteristics in cross-stream direction

To formulate a universal dissipation scaling, the flow characteristics in the cross-stream direction are analyzed at different streamwise locations within the production region (x/x_{peak} = 0.5), peak location (x/x_{peak} = 1), and the results are compared with those in the decay region (x/x_{peak} = 2). Figure 8 presents an assessment of the probability density function (pdf) of the streamwise fluctuating velocity in the production region, peak location, and decay region for both grids. Gaussian distribution (solid line) is also plotted for comparison. The figure shows that, regardless of the blockage ratio, the distributions are non-Gaussian in the production region, but nearly Gaussian in the decay region. For F32 and F41, the distribution in the peak location is similar to those in the decay and production regions, respectively. For both grids, the distribution in the production region is negatively skewed, which suggests that extreme negative fluctuation values are more likely to occur than positive ones in the production region.

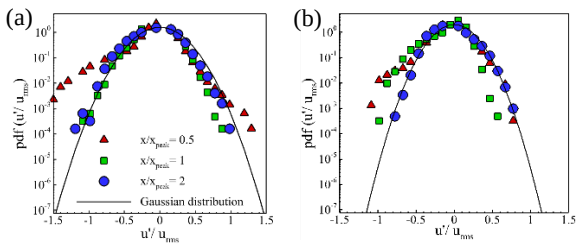

Figure 8. The pdf of the streamwise fluctuating velocity in production, peak, and decay region for F32 (a), and F41(b). The solid lines represent the Gaussian profile.

To examine the cause of the non-Gaussian distribution of fluctuating velocity observed in the production region (Figure 8), the pdf of the fluctuating vorticity at the same three streamwise locations is examined in Figure 9. Because of similarity, plots for F32 are not shown for conciseness. The pdf distribution in the production region and peak location exhibits broader tails compared to a Gaussian distribution, which is a characteristic feature of coherent structures (Wilczek et al., 2012). Conversely, a significant portion of the samples in the decay region exhibit lower vorticity levels, which stems from infrequent occurrences of coherent structures.

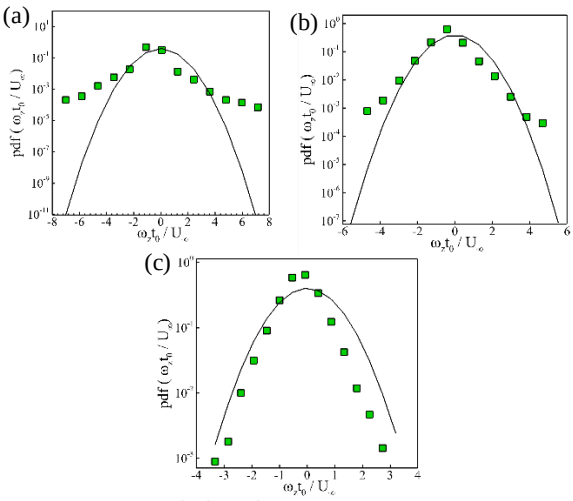

Figure 9. The pdf of the fluctuating vorticity measured at production (a), peak (b), and decay region (c) for F41. The solid lines represent the Gaussian profile.

The reduced form of the fluctuating velocity gradient tensors derived from the two-component two-dimensional PIV data is used to compare the level of the local (small-scale) isotropy (Perry and Chong, 1987):

$$\tilde{a} = \begin{bmatrix} \frac{\partial u'}{\partial x} & \frac{\partial u'}{\partial y} \\ \frac{\partial v'}{\partial x} & \frac{\partial v'}{\partial y} \end{bmatrix} \qquad (6)$$

Cardesa et al. (2013) showed that the joint probability density function (jpdf) of the two invariants of $\tilde{a}$, i.e., p = -tr ($\tilde{a}$) and q = det ($\tilde{a}$) depicts a teapot-like form around the discriminant $q/p^2 = 1/4$ which is a universal feature of turbulent flows. They also demonstrated that under local conditions characterized by small-scale isotropy, the relationship $\overline{pq} \approx 1.17\ \overline{p^3}$ holds. Table 2 provides the values of $\overline{pq}/\overline{P^3}$ at the selected streamwise locations along the grid centerline for the different grids. The data in the table show that the condition for local isotropy is not met in the production region (x/x_{peak} = 0.5) and at the peak location (x/x_{peak} = 1). In the decay region, on the other hand, the data for the grids indicate a close adherence to local isotropy.

Table 2. The ratio of $\overline{pq}/\overline{P^3}$.

	x/x_{peak} = 0.5	x/x_{peak} = 1	x/x_{peak} = 2
F32	0.06	0.65	1.17
F41	0.36	3.02	1.21

Scaling of C_ε in the cross-stream direction

Given the observed anisotropy in the production region and location of peak production, following Chen et al. (2021), a new dissipation rate coefficient ($C_{\varepsilon'}$) and turbulence Reynolds number ($Re_{\lambda'}$) are defined as follows:

$$C_{\epsilon'} = \varepsilon \langle L_u \rangle / J^3 \qquad (7)$$

$$Re_{\lambda'} = \lambda J / \upsilon \qquad (8)$$

In these equations, $J = \sqrt{2/3\,k}$, where $k = 0.5(\overline{u'u'}+\overline{v'v'})$, and $<L_u>$ denotes the spatial average of the longitudinal integral length scale in the cross-stream direction. It should be noted that the longitudinal integral length scale is determined by the integration of the spatial two-point auto-correlation function of streamwise fluctuating velocity (Equation 9). The streamwise separation between these points is denoted as r_x. In Equation 10, r_0 is identified as the point where the two-point auto-correlation coefficient R initially crosses zero.

$$R(x, y, r_x) = \frac{\overline{u'(x,y)u'(x+r_x,y)}}{\sqrt{\overline{u'(x,y)^2}}\sqrt{\overline{u'(x+r_x,y)^2}}} \qquad (9)$$

$$L_u(x,y) = \int_0^{r_0} R(x, y, r_x)\, dr_x \qquad (10)$$

Figure 10 shows the cross-stream distribution of $C_{\epsilon'}$ versus $Re_{\lambda'}$ for the grids at various streamwise locations within the production region, peak location, and decay region. In each figure, a power law function ($C_{\epsilon'} \propto Re_{\lambda'}^{-n}$), and the R-squared value for the fit is provided. It is evident that, regardless of the solidity, an inverse relationship exists between the energy dissipation rate coefficient and turbulence Reynolds number in the cross-stream direction, both in the production region and at the peak location. In the decay region, $C_{\epsilon'}$ tends to be independent of $Re_{\lambda'}$, which aligns with findings from previous studies (Takamure et al., 2019). The data show a reasonably good fit with power law, with R-squared values between 0.71 and 0.98. Notably, the power-law exponent is identical for both grids in the production region and peak location. As equilibrium $C_{\epsilon'}$ is dependent on the inlet flow conditions (Antonia and Pearson, 2000), its value differs for the different grids, i.e., $C_{\epsilon'} \approx 0.62$, and 0.55 for F32 and F41, respectively.

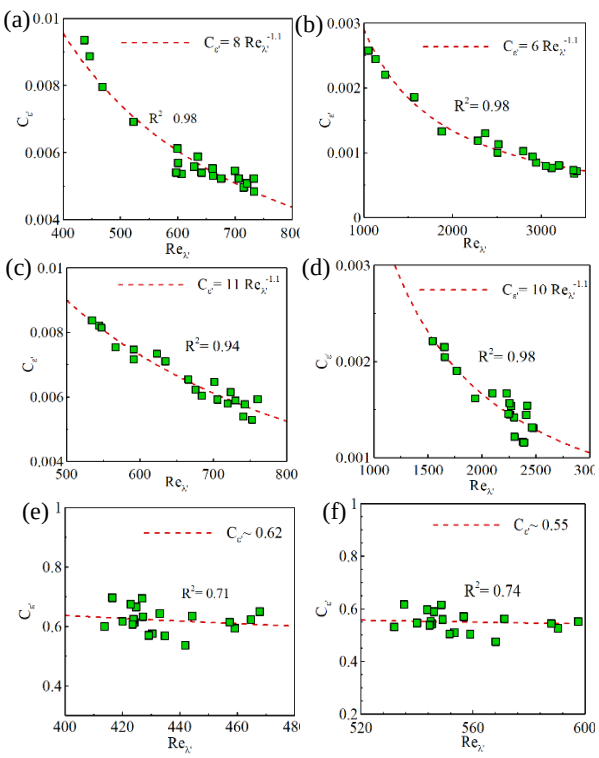

Figure 10. Scatter plots of $C_{\epsilon'}$ versus $Re_{\lambda'}$ values in cross-stream direction at $x/x_{peak} = 0.5$ [(a) and (b)] and $x/x_{peak} = 1$[(c) and (d)] and decay region [(e) and (f)] for F32 [(a), (c) and (e)], F41 [(b), (d) and (f)].

To find a universal relation between the $C_{\epsilon'}$ and $Re_{\lambda'}$ in the production region, a new global Reynolds number is proposed as follows:

$$Re_L = J<L_u>/\upsilon \qquad (11)$$

By carefully examining the equations and deriving a universal equation similar to Equation 4, it is possible to relate $C_{\epsilon'}$ to the proposed global Reynolds number in the production region and peak location. Figure 11 shows the plots of $C_{\epsilon'}Re_{\lambda'}$ versus Re_L in logarithmic scale for F32 and F41 in the peak and production regions. The dashed line with a slope of -1 is also superimposed on the figure, demonstrating an inverse relationship between $C_{\epsilon'}Re_{\lambda'}$ and Re_L. This relation was also observed for other streamwise locations within the production region. Based on the figure, it can be concluded that a new non-equilibrium equation, $C_{\epsilon'} \propto Re_L^m / Re_{\lambda'}^n$, holds for grids in the anisotropic and inhomogeneous regions. The appropriate power exponents are $m \approx -0.2$ and $n \approx 1$. The observed inverse relationship between $C_{\epsilon'}$, $Re_{\lambda'}$ and Re_L in the peak and production regions indicates that as the global Reynolds number (Re_L) increases (decreases), the product of the local Reynolds number ($Re_{\lambda'}$) and the dissipation rate coefficient ($C_{\epsilon'}$) decreases (increases). The proposed non-equilibrium equation provides a valuable tool to predict the TKE dissipation rate coefficient in anisotropic and inhomogeneous regions.

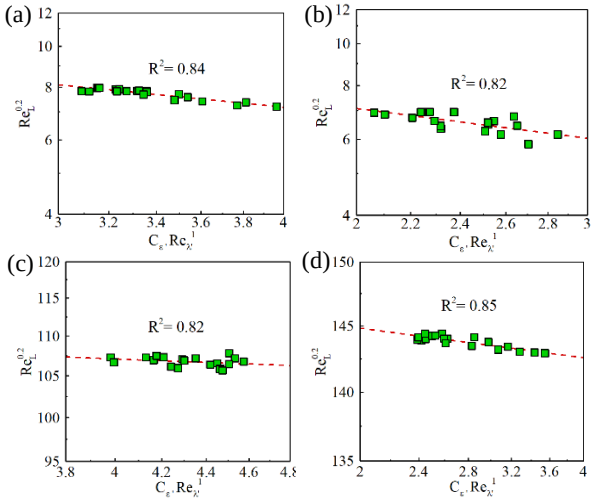

Figure11. Scatter plots of $C_{\epsilon'}Re_{\lambda'}^n$ in relation to Re_L^m at $x/x_{peak} = 0.5$ [(a), (b)] and $x/x_{peak} = 1$[(c), (d)] for F32 [(a) and (c)] and F41[(b) and (d)]. The dashed line represents $C_{\epsilon'}Re_{\lambda'}^n \propto Re_L^m$ with slope = -1.

CONCLUSION

This study provided a detailed examination of turbulence downstream of fractal grids using particle image velocimetry. Two fractal grids with different blockage ratios, σ = 32% and 41% (F32 and F41, respectively) were examined. Analysis of the mean velocity downstream of the grids indicates that grids with higher blockage ratios (F41) exhibit higher streamwise mean velocity and streamwise turbulence intensity in the production region. The probability density functions of velocity and vorticity fluctuations indicate that flow in the cross-stream direction within the production region and peak location is anisotropic and inhomogeneous. An inverse relationship was observed between $C_{\epsilon'}$ and $Re_{\lambda'}$ in the cross-stream direction within the production and peak locations. A

non-equilibrium scaling, $C_{\epsilon'} \propto {Re_L^m}/{Re_{\lambda'}^n}$, was proposed for the production region and peak location, downstream of the grids. This new dissipation rate coefficient scaling holds for flow downstream of both fractal grids with the exponents $m \approx -0.2$ and $n \approx 1$, regardless of grid blockage ratios.

Acknowledgment

The authors acknowledge the support of this work by the Natural Sciences and Engineering Research Council of Canada (NSERC) to M.F.T. We are also grateful to the Canada Foundation for Innovation (CFI) for funding the experimental facility.

REFERENCES

Antonia, R.A. and Pearson, B.R., 2000, "Effect of initial conditions on the mean energy dissipation rate and the scaling exponent", *Physical Review E*, Vol. 62, p.8086.

Azzam, A. and Lavoie, P., 2023, "Unsteady flow generation in a wind tunnel using an active grid", *Experiments in Fluids*, Vol. 64, p.29.

Bos, W.J. and Rubinstein, R., 2017, "Dissipation in unsteady turbulence", *Physical Review Fluids*, Vol. 2, p.022601.

Cafiero, G., Castrillo, G. and Astarita, T., 2021, "Turbulence properties in jets with fractal grid turbulence", *Journal of Fluid Mechanics*, Vol. 915, p.A12.

Cafiero, G. and Vassilicos, J.C., 2019, "Non-equilibrium turbulence scalings and self-similarity in turbulent planar jets", *Proceedings of the Royal Society A*, 475, p.20190038.

Cardesa, J.I., Mistry, D., Gan, L. and Dawson, J.R., 2013, "Invariants of the reduced velocity gradient tensor in turbulent flows", *Journal of Fluid Mechanics*, Vol. 716, pp.597-615.

Chen, J. G., Cuvier, C., Foucaut, J. M., Ostovan, Y., and Vassilicos, J. C., 2021, "A turbulence dissipation inhomogeneity scaling in the wake of two side-by-side square prisms", *Journal of Fluid Mechanics*, Vol. 924, A4.

Ferko, K., Chiappazzi, N., Gong, J. and Danesh-Yazdi, A.H., 2019, "Power output comparison of side-by-side fluidic harvesters in different types of fractal grid-generated turbulence", In *Active and Passive Smart Structures and Integrated Systems XIII*, Vol. 10967, pp. 166-176.

Fuchs, A., Medjroubi, W., Hochstein, H., Gülker, G. and Peinke, J., 2022, "Experimental and Computational Investigation of a Fractal Grid Wake", *arXiv preprint arXiv:2210.06208*.

Goto, S. and Vassilicos, J.C., 2016, "Local equilibrium hypothesis and Taylor's dissipation law", *Fluid Dynamics Research*, Vol. 48, p.021402.

Hearst, R. J., 2015, *Fractal, classical, and active grid turbulence: From production to decay*, Ph.D. thesis, University of Toronto, Toronto.

Hurst, D., and Vassilicos, J.C., 2007, "Scalings and decay of fractal-generated turbulence", *Physics of Fluids*, Vol. 19, pp. 1-31.

Isaza, J.C., Salazar, R. and Warhaft, Z., 2014, "On grid-generated turbulence in the near- and far field regions", *Journal of Fluid Mechanics*, Vol. 753, pp.402-426.

Kang, H.S., Chester, S. and Meneveau, C., 2003. "Decaying turbulence in an active-grid-generated flow and comparisons with large-eddy simulation", *Journal of Fluid Mechanics*, Vol. 480, pp.129-160.

Laizet, S. and Vassilicos, J.C., 2012, "Fractal space-scale unfolding mechanism for energy-efficient turbulent mixing", *Physical Review E*, Vol. 86, p.046302.

Melina, G., Bruce, P. J., and Vassilicos, J. C., 2016 "Vortex shedding effects in grid-generated turbulence", *Physical Review Fluids*, Vol. 1, pp. 044402.

Nagata, K., Sakai, Y., Inaba, T., Suzuki, H., Terashima, O. and Suzuki, H., 2013, "Turbulence structure and turbulence kinetic energy transport in multiscale/fractal-generated turbulence", *Physics of Fluids*, Vol. 25.

Nedić, J. and Vassilicos, J.C., 2015, "Vortex shedding and aerodynamic performance of airfoil with multiscale trailing-edge modifications", *AIAA Journal*, Vol. 53, pp. 3240-3250.

Obligado, M., Brun, C., Silvestrini, J.H. and Schettini, E.B.C., 2022, "Dissipation Scalings in the Turbulent Boundary Layer at Moderate Re_θ", *Flow, Turbulence and Combustion*, Vol. 108, pp.105-122.

Ortiz-Tarin, J.L., Nidhan, S. and Sarkar, S., 2021, "High-Reynolds-number wake of a slender body", *Journal of Fluid Mechanics*, Vol. 918, p.A30.

Perry, A.E. and Chong, M.S., 1987, "A description of eddying motions and flow patterns using critical-point concepts", *Annual Review of Fluid Mechanics*, Vol. 19, pp.125-155.

Poorte, R.E.G. and Biesheuvel, A., 2002, "Experiments on the motion of gas bubbles in turbulence generated by an active grid", *Journal of Fluid Mechanics*, Vol. 461, pp.127-154.

Pope, S. B., 2000, "Turbulence Flows", *Cambridge University Press*.

Puga, A.J. and LaRue, J.C., 2017, "Normalized dissipation rate in a moderate Taylor Reynolds number flow", *Journal of Fluid Mechanics*, Vol. 818, pp.184-204.

Samimy, M. and Lele, S.K., 1991, "Motion of particles with inertia in a compressible free shear layer", *Physics of Fluids A: Fluid Dynamics*, Vol. 3, pp.1915-1923.

Takamure, K., Sakai, Y., Ito, Y., Iwano, K. and Hayase, T., 2019, "Dissipation scaling in the transition region of turbulent mixing layer", *International Journal of Heat and Fluid Flow*, Vol. 75, pp.77-85.

Tokgoz, S., Elsinga, G.E., Delfos, R. and Westerweel, J., 2012, "Spatial resolution and dissipation rate estimation in Taylor--Couette flow for tomographic PIV", *Experiments in fluids*, Vol. 53, pp. 561-583.

Vassilicos, J.C., 2015, "Dissipation in turbulent flows", *Annual review of fluid mechanics*, Vol. 47, pp.95-114.

Weitemeyer, S., Reinke, N., Peinke, J. and Hölling, M., 2013, "Multi-scale generation of turbulence with fractal grids and an active grid", *Fluid Dynamics Research*, Vol. 45, p.061407.

Wilczek, M., Kadoch, B., Schneider, K., Friedrich, R. and Farge, M., 2012, "Conditional vorticity budget of coherent and incoherent flow contributions in fully developed homogeneous isotropic turbulence", *Physics of Fluids*, Vol. 24.

Zheng, Y., Nagata, K. and Watanabe, T., 2021, "Turbulent characteristics and energy transfer in the far field of active-grid turbulence", *Physics of Fluids*, Vol. 33.

Zheng, Y., Nakamura, K., Nagata, K. and Watanabe, T., 2023, "Unsteady dissipation scaling in static-and active-grid turbulence", *Journal of Fluid Mechanics*, Vol. 956, p. A20.